Chapter 2
3D Force Field Spectroscopy

Mehmet Z. Baykara and Udo D. Schwarz

Abstract With recent advances in instrumentation and experimental methodology, noncontact atomic force microscopy is now being frequently used to measure the atomic-scale interactions acting between a sharp probe tip and surfaces of interest as a function of three spatial dimensions, via the method of *three-dimensional atomic force microscopy* (3D-AFM). In this chapter, we discuss the different data collection and processing approaches taken towards this goal while highlighting the associated advantages and disadvantages in terms of correct interpretation of results. Additionally, common sources of artifacts in 3D-AFM measurements, including thermal drift, piezo nonlinearities, and tip-related issues such as asymmetry and elasticity are considered. Finally, the combination of 3D-AFM with simultaneous scanning tunneling microscopy (STM) is illustrated on surface-oxidized Cu(100). We conclude the chapter by an outlook regarding the future development of the 3D-AFM method.

2.1 Introduction

A complete and accurate understanding of the atomic structure of solids as well as their physical properties related to interatomic interactions and bonding are required for the successful development of new applications based on emerging phenomena such as superconductivity and molecular electronics. In this context, the physical properties of solid surfaces on the atomic scale are of primary concern due to the fact that the interaction of materials with other atoms and molecules in their vicinity via surfaces define their functionality for various applications from wear-resistant and low-friction coatings to microelectronics. The capability of imaging solid surfaces in

M.Z. Baykara (✉)
Department of Mechanical Engineering and UNAM-Institute of Materials Science and Nanotechnology, Bilkent University, 06800 Ankara, Turkey
e-mail: mehmet.baykara@bilkent.edu.tr

U.D. Schwarz
Center for Research on Interface Structures and Phenomena (CRISP), Department of Mechanical Engineering and Materials Science, Department of Chemical and Environmental Engineering, Yale University, New Haven 06520, USA
e-mail: udo.schwarz@yale.edu

S. Morita et al. (eds.), *Noncontact Atomic Force Microscopy*,
NanoScience and Technology, DOI 10.1007/978-3-319-15588-3_2

real space with atomic resolution was established with the invention of the scanning tunneling microscope (STM) in the early 1980s [1], and the subsequent development of the atomic force microscope [2] allowed nanometer-scale imaging of surfaces without limitations regarding conductivity [3]. Eventually, thanks to the development of the *noncontact* operation mode of AFM (NC-AFM) [4–7] based on a frequency-modulation approach involving oscillating cantilevers [8], true atomic-resolution imaging was achieved over the last two decades on a large array of material surfaces, ranging from ionic crystals [9–11], metals [12–14] and metal oxides [15] to the new class of *two-dimensional* materials, including graphene [16, 17] and silicene [18].

Atomic-resolution imaging of materials has initially been the primary focus of NC-AFM; shortly after its successful demonstration, however, scientists already started to direct parts of their efforts to the measurement of site-specific interactions using the method of *dynamic force spectroscopy* (DFS) [19–21]. Based on the idea of collecting *frequency shift* (Δf) information—the main signal utilized for atomic-resolution imaging in NC-AFM—as a function of tip-sample separation on atomically defined sites of the material surface under investigation, DFS allows the conversion of the acquired data to *force-distance* as well as *energy-distance* curves via mathematical procedures performed post-data-acquisition [22]. While the DFS technique allows the acquisition of single interaction curves on defined lattice sites as indicated, converting the method into a comprehensive tool capable of collecting full *three-dimensional* (volumetric) maps of interaction forces and energies with atomic resolution took considerable effort due to limitations in terms of various experimental factors including tip and sample stability, as well as thermal drift. Eventually, thanks to advancements in instrumentation and experimental methodology such as low temperature operation [23] and atom-tracking/feedforward methods [24, 25], the method of *three-dimensional atomic force microscopy* (3D-AFM) was established, implementation of which has now successfully been demonstrated by various research groups on a variety of sample surfaces [26–37]. Originally developed for vacuum conditions, the method has recently been extended to operation under liquid environments, thereby opening up tremendous possibilities for high-resolution investigation of biological material under close-to-natural conditions [38–40]. Despite the exciting potential of 3D force field spectroscopy in liquids, a related discussion is beyond the scope of this chapter, as we will solely focus on atomic-resolution spectroscopy experiments performed under ultrahigh vacuum.

Despite the recent success of the 3D-AFM method in acquiring atomic-resolution, volumetric maps of interaction forces and energies on a steadily growing list of materials, the experimental approaches used to collect the related data have not been standardized. Moreover, the technique frequently suffers from various artifacts related to thermal drift and piezo nonlinearities, as well as tip-related issues involving elasticity and asymmetry [41, 42]. In this chapter, we will review the advantages and disadvantages of the particular methods proposed in the literature to perform 3D-AFM and analyze the effect of different artifacts on the measurements. Moreover, the extension of the capabilities of the 3D-AFM method in terms of the collected physical information will be demonstrated via simultaneous 3D-AFM/STM measurements performed on surface-oxidized Cu(100) [36].

2.2 Experimental Methodology

The essential goal of any scanning probe microscopy (SPM) method (including AFM and STM) is to collect accurate information about the physical properties of the investigated surface. On the other hand, the information collected via such an approach will, to a certain extent, be always influenced by the specifics of the experimental methodology utilized to perform data acquisition as well as the physical properties of the probe itself. Within that context, we will review in this section the common methods reported in the literature to perform atomic-resolution 3D-AFM. The following section will then deal with the effect of various artifact sources on collected information. Finally, the methods reported here to perform 3D-AFM will be compared and contrasted with respect to the extent to which they are influenced by the discussed artifacts.

The most commonly reported methods in the literature to perform 3D-AFM may be considered under two general categories (Fig. 2.1):

(a) The *curve-by-curve* method, involving the recording of individual curves of frequency shift as a function of tip-sample distance ($\Delta f(z)$) at a number of lateral (x, y) locations on the sample surface [30, 31, 33–35, 37]. The curves are then

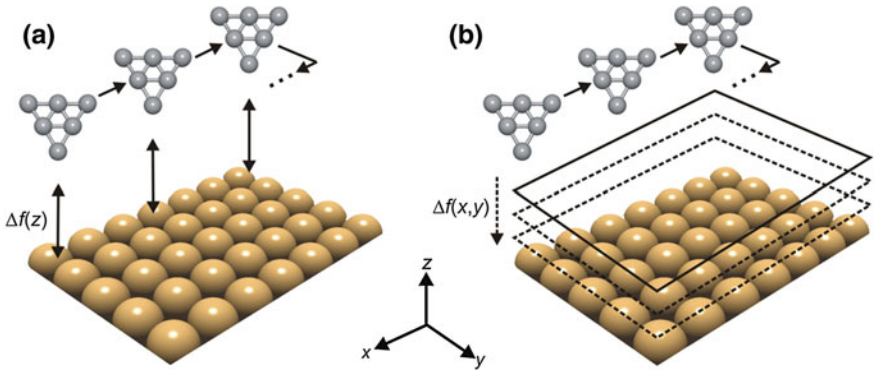

Fig. 2.1 Schematic illustrations describing the *curve-by-curve* (**a**) and the *layer-by-layer* (**b**) approaches taken towards 3D force field spectroscopy. While individual $\Delta f(z)$ curves are recorded in (**a**), consecutive NC-AFM images at fixed setpoints above the surface are collected in (**b**). Image reproduced from [41]

combined such that full three-dimensional maps of frequency shift ($\Delta f(x, y, z)$) are formed that are subsequently converted to interaction force ($F(x, y, z)$) and energy ($E(x, y, z)$) maps [22].

(b) Utilizing an alternative approach, the volumetric $\Delta f(x, y, z)$ data may be recorded in a *layer-by-layer* fashion, by combining a group of *topographical* NC-AFM images that contain $\Delta f(x, y)$ data for set tip-sample distances z [26, 29, 31, 32, 36]. Volumetric maps of interaction force ($F(x, y, z)$) and energy ($E(x, y, z)$) are then obtained via the same procedures employed for the *curve-by-curve* approach [22].

While the *curve-by-curve* method relies on conventional procedures established for dynamic force spectroscopy (DFS) to collect individual $\Delta f(z)$ curves, the *layer-by-layer* method necessitates a more involved data acquisition and processing procedure (Fig. 2.2), which will be briefly reviewed here (for details, see [43]).

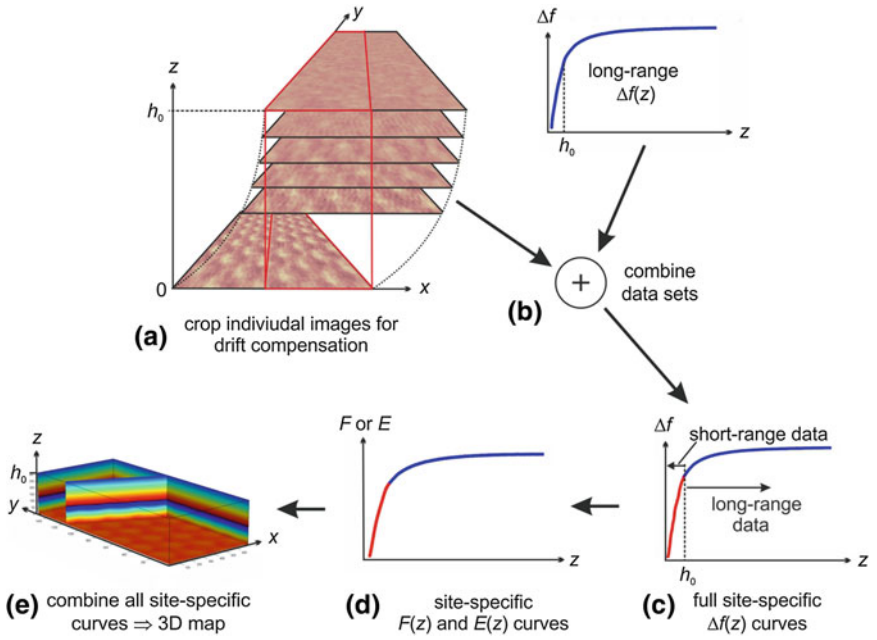

Fig. 2.2 Overview of the data processing steps involved in 3D force field spectroscopy via the *layer-by-layer* approach. **a** After slight Fourier filtering to remove high frequency noise, the individual images are laterally adjusted with respect to each other to correct for drift. Data outside the area where all recorded images overlap (indicated by the *red lines*) are cropped. **b** Long-range data from an individually collected $\Delta f(z)$ curve (i.e., data covering tip–sample separations $> h_0$) are added to the site-specific short-range curves for each lateral position (x, y) recovered from the images. The full $\Delta f(z)$ curves obtained in this fashion (**c**) are converted into $F(z)$ or $E(z)$ *curves* (**d**). Finally, all $F(z)$ and $E(z)$ curves are combined to form three-dimensional maps of $F(x, y, z)$ or $E(x, y, z)$, respectively (**e**). Image reproduced from [43]

The data acquisition procedure for 3D force field spectroscopy via the *layer-by-layer* approach involves the following steps:

- The sample surface is first imaged via regular (*topographical*) NC-AFM at a fixed frequency shift setpoint Δf. During imaging, the topography feedback is kept on to prevent sudden crashes of the tip with the sample surface. While imaging the surface, topography z as well as frequency shift Δf data for each lateral position (x, y) (which frequently vary to a small extent from the fixed setpoint due to non-perfect operation of the feedback loop) are recorded. Additional data channels recorded during imaging may include the oscillation amplitude A, the excitation amplitude A_{exc}, as well as tunneling current I in case of a (semi-)conducting sample.
- Following the recording of a given image as indicated above, the imaging setpoint for Δf is decreased, the tip-sample distance consequently increases, and a new image is recorded at the new setpoint.
- New images are recorded at subsequent setpoints until atomic-scale contrast vanishes (at a given height h_0), as following images at even lower setpoints will then contain the same, non-site-specific information.
- Additionally, individual $\Delta f(z)$ curves are recorded before and after data acquisition to (i) re-confirm that no tip changes have occurred during data collection and (ii) to calculate the non-site-specific (*long-range*) part of the tip-sample interaction, as explained in the following parts of the present section.

A couple of aspects that need to be mentioned in terms of data acquisition include (i) that the vertical distance between consecutive images is not constant and changes with the local slope of $\Delta f(z)$ and (ii) that the specific performance of the topography feedback loop (and associated deviations from the setpoint Δf during imaging) does not have a significant effect on the measurement since the Δf and z data for each lateral position (x, y) are later combined.

Once data collection is performed as indicated above, the collected information is subjected to several processing steps to eventually obtain three-dimensional $F(x, y, z)$ and $E(x, y, z)$ maps. The individual data processing steps may be summed up as:

- *Low-Pass Fourier Filtering*: The topographical (z) and frequency shift (Δf) maps collected are slightly low-pass filtered to remove any high-frequency noise in the data. Care is taken to ensure that the cut-off wavelength is significantly smaller than the interatomic spacing on the surface.
- *Removing Lateral Drift*: The lateral shift between subsequent images due to thermal drift (significantly reduced but not completely removed even for low-temperature measurements due to the long data acquisition times associated with the technique on the order of multiple hours) is determined by inspection and manually removed by shifting all individual images (of z and Δf) laterally in the xy plane. Only the pixels that overlap for all images are kept, and the rest of the images are then cropped accordingly (Fig. 2.2a).

- *Combining Short-Range and Long-Range Interactions*: To recover interaction force/energy information from frequency shift data, $\Delta f(z)$ information needs to be available, from the tip–sample distance that one is interested in, all the way back to where interactions are negligible [22]. As such, the short-range $\Delta f(z)$ information collected for each lateral position (x, y) in the previous steps needs to be combined with the long-range, non-site specific part of the interaction, that is the same for all lateral positions (x, y) in the data set above h_0. Towards this purpose, the tail of the long-range $\Delta f(z)$ curves (at $z > h_0$) recorded before and after *layer-by-layer* data acquisition is added on to the site-specific short-range $\Delta f(z)$ information recorded for each lateral position via the steps discussed above (Fig. 2.2b, c).
- *Calculation of 3D Force/Energy Maps*: In the final step of data processing for the *layer-by-layer* method, complete $\Delta f(z)$ curves calculated in the previous step are converted to $F(z)$ and $E(z)$ curves via the mathematical procedures established in the literature [22] and the individual curves for each (x, y) position (Fig. 2.2d) are combined to form full 3D maps of interaction force ($F(x, y, z)$) and energy ($E(x, y, z)$) (Fig. 2.2e).

It should be noted here that for the *layer-by-layer* approach to be applied in a feasible manner, the lateral as well as vertical drifts acting between the tip and sample need to be minimized. As such, the technique requires either low temperature operation [23] or the utilization of atom-tracking/feedforward methodologies [24, 25] for proper execution.

2.3 Sources of Artifacts in 3D Force Field Spectroscopy

All SPM measurements are influenced to a certain extent by artifacts affecting imaging and spectroscopy. While some artifact sources are due to the specifics of the instrumentation used in the measurements (such as thermal drift, piezo nonlinearities, etc.), others are intimately related to the physical properties of the probe itself (such as asymmetry, elasticity as well as chemical identity of the apex). In this section, we will review each source of artifact relevant for 3D force field spectroscopy measurements and evaluate its effect on acquired data.

2.3.1 Thermal Drift

As all scanning probe microscopes ultimately feature components that are made of different materials with varying thermal expansion coefficients, relative motion of the sample with respect to the probe tip due to changes in temperature (the phenomenon of *thermal drift*) are inevitable. Taking into account that performing 3D force field spectroscopy typically involves data acquisition over multiple hours, artifacts related to thermal drift become significant. Specifically, measurements performed at room

temperature as opposed to low temperatures (corresponding to liquid nitrogen or helium temperatures) may typically feature drift rates of several Å per minute. On the other hand, operation at, e.g., liquid helium temperatures may severely reduce drift rates (as low as a few Å per day, [23]).

Despite the impractically large drift rates typically experienced by scanning probe microscopes operating at room temperature, the associated problems have been largely overcome in recent years by the introduction of atom-tracking and feedforward positioning methods. Atom tracking [24] involves the determination of the three-dimensional drift vector by considering the shift in the position of an individual maximum in subsequently recorded SPM images followed by an appropriate correction of the tip location that compensates for this drift. In contrast, the feedforward procedure [25] is based on the real-time correction of drift during data acquisition by applying appropriate voltages to the scan piezo, which are predicted by relying on the assumption that the drift vector can be adequately determined in prior measurements. Both approaches have been successfully implemented in the past to perform 3D force field spectroscopy at room temperature and low temperatures on various sample surfaces [30, 31, 33–35, 37]. One potential shortcoming of the method is the fact that the drift vector may need to be frequently updated during actual measurements based on the unpredictability of thermal fluctuations and associated drift rates. Lateral thermal drift rates of more than one unit cell in the time required to collect a single image also prove to be problematic, limiting *layer-by-layer* data acquisition to low temperatures [31].

As explained in Sect. 2.2 of this chapter, lateral drift correction may be performed post-data-acquisition via manual lateral shifting of subsequent images with respect to each other, as part of the *layer-by-layer* 3D force field spectroscopy approach [26, 36, 43]. With a sufficiently dense dataset consisting of images separated by only a few picometer in the z direction, gradual lateral shifts between subsequent images due to thermal drift may be precisely monitored and corrected for provided that lateral drifts between images are significantly lower than one unit cell.

It should be noted that thermal drift is not limited to lateral dimensions, but also affects the tip-sample separation in the vertical direction. Fortunately, certain basic procedures can be employed to eliminate the effect of z drift on force field spectroscopy. For volumetric maps obtained using the *curve-by-curve* method, such drift-induced distortions can be corrected via standard algorithms involving line-fitting etc. When the *layer-by-layer* approach is utilized, the necessary adjustments can be carried out by comparison with site-specific $\Delta f(z)$ calibration curves recorded directly before and/or after the individual layers needed to assemble the actual data array.

2.3.2 Piezo Nonlinearities

Modern scanning probe microscopes rely on components made out of piezoelectric materials for precise (picometer-scale) positioning of the probe tip with respect to

the sample surface in the three spatial dimensions [44]. Despite their widespread use in almost every SPM system, piezoelectric positioning systems suffer from a number of material-related complications including piezo nonlinearities leading to problems associated with *hysteresis* and *creep*, which ultimately may affect 3D force field measurements in the form of distorted images [3].

Solutions aimed at the correction/prevention of artifacts associated with piezo nonlinearities include tracking the actual position of tip/sample with external deflection sensors in real time or the application of voltages in the form of distorted waveforms so that the resulting motion is linear with respect to voltage [44, 45]. Atom-tracking and feedforward techniques, successful in correcting the effects of thermal drift, also help alleviate artifacts associated with piezo nonlinearities. Alternative strategies include: (i) post-data-acquisition correction of lattice distortions in atomic-resolution images using the known size and symmetry of surface unit cells [46], (ii) waiting a certain amount of time between the recording of each curve/image to reduce piezo creep, and (iii) operation at low temperatures, which is known to reduce the extent of piezo nonlinearities [47].

Despite the fact that artifacts related to the nonlinear behavior of piezoelectric positioning elements may not be completely suppressed using a straightforward approach, operation at low temperatures emerges as an ideal strategy with regards to 3D force field spectroscopy when the additional effect of reduced thermal drift is considered [23].

2.3.3 Tip Asymmetry

Despite the remarkable success of NC-AFM in measuring the atomic-scale structure of surfaces as well as associated interaction forces/energies via 3D force field spectroscopy, an important but often overlooked shortcoming of the technique is the inadvertent effect of structural and chemical properties of the tip apex (such as tip asymmetry, elasticity or elemental composition) on acquired data [36, 41, 42, 48–51]. Since most tip apices used in 3D force field spectroscopy feature a certain degree of atomic-scale asymmetry at the very apex with respect to the surface due to the methods by which they are obtained, significant inconsistencies arise between different experiments performed on the same sample system by different research groups or even by the same research group on different occasions. As such, a comprehensive understanding of tip asymmetry and its effect on 3D force field spectroscopy is a prerequisite for correct interpretation of obtained results.

Motivated by the discussion above, we will present in this part of the chapter an investigation of the effect of *tip apex asymmetry* on 3D force field spectroscopy via numerical simulations using the model sample surface of Cu(001) (Fig. 2.3a) and model, two-dimensional tip apices consisting of six Pt atoms arranged in a close-packed configuration (Fig. 2.3b, c). Significant asymmetry in the tip apex structure is obtained by rotating the apex by an angle θ around the frontmost atom (Fig. 2.3c). Force interactions between each tip and sample atom for the symmetric

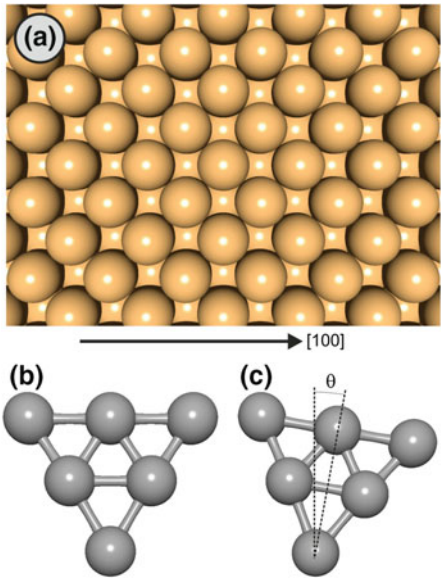

Fig. 2.3 (**a**) The *hard sphere* model of the Cu(001) surface employed in the numerical simulations regarding the effect of tip asymmetry on 3D force field spectroscopy. Symmetric (**b**) and asymmetric (**c**) tip apex models consisting of 6 Pt atoms in close-packed configuration are depicted, as well. Note that varying degrees of asymmetry in the tip apex are induced by rotating the symmetric apex model by an angle θ around the frontmost atom. Image reproduced from [41]

and asymmetric tip apices are calculated using a 12-6 Lennard-Jones (L-J) model with appropriate parameters for Cu and Pt atoms as well as Lorentz-Berthelot mixing rules [41]. Finally, the total normal force interaction experienced by the tip is plotted as a function of lateral position and tip-sample distance along the [100] crystallographic direction via 2D maps of force on the (x, z) plane (Fig. 2.4).

For a symmetric tip apex (i.e., $\theta = 0°$), force maxima are directly located above Cu atoms and evolve in a symmetric fashion as the tip-sample distance is increased (Fig. 2.4a). Please note that at very close separations, force maxima switch from atomic positions to hollow sites between the atoms, essentially pointing to a crossing of the $\Delta f(z)$ curves recorded above the atomic and hollow sites at small tip-sample separations, similar to the one previously observed in simulations carried out for a xenon (111) surface [52]. On the other hand, when asymmetric tips ($\theta = 45°$ and $\theta = 58°$) are used to simulate force field spectroscopy on the surface (Fig. 2.4b, c), force field maxima associated with the surface become increasingly *lopsided* (much like the data acquired on graphite and presented in [53]) and a significant offset between the locations of perceived force maxima and the (x, y) positions of the surface copper atoms develops with decreasing tip-sample distance.

Consequently, let us note that when the *layer-by-layer* approach is employed to perform 3D force field spectroscopy in conjunction with manual post-data-acquisition drift correction, the fact that the location of the maximum attractive force smoothly moves from the atomic to the hollow sites upon decreasing the tip-sample distance

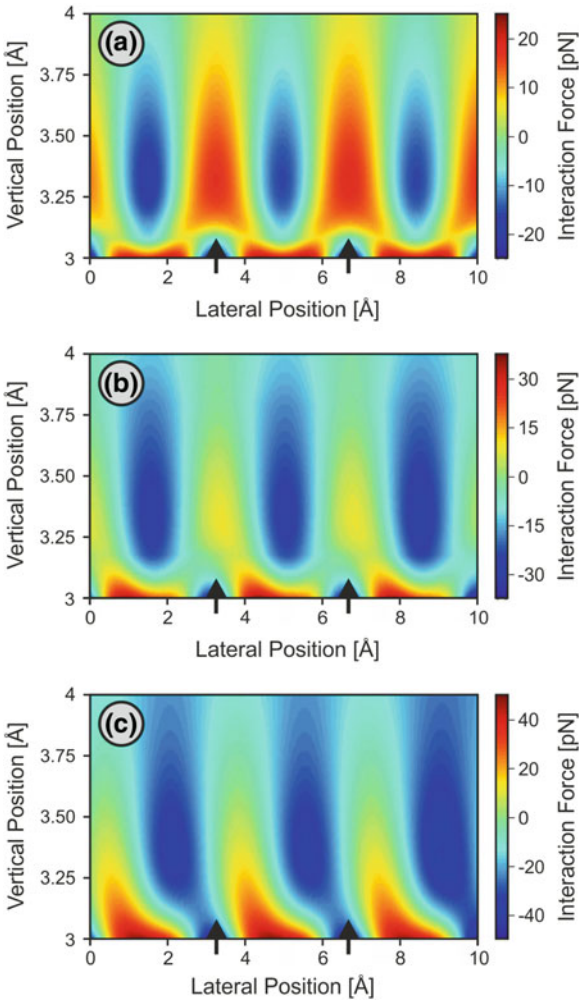

Fig. 2.4 2D maps of normal interaction forces simulated over the model Cu(001) surface along the [100] direction for symmetric (**a** $\theta = 0°$) and asymmetric (**b** $\theta = 45°$; **c** $\theta = 58°$) tip apices illustrated in Fig. 2.3b, c. The difference between the interaction force at each point and the mean interaction force at that height is displayed for better contrast visibility. The vertical axis indicates the distance in z direction between the center of the front-most tip atom and the centers of the surface copper atoms. *Black arrows* mark the lateral positions of surface Cu atoms. Image reproduced from [41]

for the sample surface of Cu(001) can be particularly problematic, as the associated effect cannot readily be distinguished from thermal drift or lateral shifting due to overall elastic bending of the probe tip. On the other hand, similar simulations performed on NaCl(001) have revealed that such effects are not observed when the dominant interactions between the probe and sample atoms are electrostatic (i.e., long-range) in character [41]. As such, the *layer-by-layer* method in conjunction with post-data-acquisition drift correction should be, to a first approximation, safely applicable to sample systems such as ionic crystals and metal oxides.

2.3.4 Tip Elasticity

In addition to tip asymmetry, an important factor affecting NC-AFM measurements in general and 3D force field spectroscopy experiments in particular is tip elasticity and associated elastic deformations of the tip apex under the influence of external forces as it is scanned over the sample surface. Elastic deformations of the tip apex may manifest in three distinct ways:

(a) Normal (i.e., vertical) forces acting on the tip apex in the attractive interaction regime will lead to an extension of the probe in the vertical direction as well as a bending and an effective overall lateral movement of the tip apex in a particular direction, if the tip used to probe the sample surface is asymmetric.

(b) Site-specific lateral forces acting on the tip apex will cause lateral shifts in its position as the tip is scanned over the surface. While such shifts are reversible and should average out while scanning along a periodic array of atoms for a given crystallographic direction, their local effect on 3D force field spectroscopy should be detectable if tips with low lateral stiffness values (k_{lateral}) are employed.

(c) Finally, lateral forces acting on the probe tip may lead to reversible (or irreversible) atomic-scale displacements at the very apex, leading to sudden changes in local tip-sample interactions.

It is important to point out here that the effect due to part (a) should be indistinguishable from that of thermal drift in the *layer-by-layer* approach since the bending of the tip towards a preferred direction at increasing setpoints would lead to a lateral shift of features with respect to each other in subsequent images. As such, the combined effects of thermal drift and (a) can be both eliminated via post-data-acquisition drift correction, highlighting a particular advantage of the *layer-by-layer* strategy for 3D force field spectroscopy.

On the other hand, the extent of (c) on 3D force field spectroscopy ultimately depends on the atomic-scale structure of the tip apex and whether atoms at particularly instable locations are to be found in a given experiment. While a discussion of associated artifacts are beyond the scope of this chapter, we will direct our attention to (b) and try to quantify the effect of site-specific lateral forces on force field spectroscopy using numerical simulations similar to those reported previously for tip asymmetry. Towards this purpose, the interactions between the model sample surface of NaCl(001) and a symmetric Pt tip apex are calculated, using a combination of L-J as well as ionic repulsion and attraction forces. Moreover, the Pt atom at the very end of the tip apex model is taken to carry a positive unit charge and the apex is considered to be connected to the rest of the microscope via a probe tip with a lateral stiffness of k_{lateral} [42].

2D maps of normal interaction forces calculated along the [100] crystallographic direction on NaCl(001) with tips having lateral stiffness values of ∞ (corresponding to a rigid tip), 25, 15, and 5 N/m are depicted in Fig. 2.5. It is clearly observed that elastic lateral deformations undergone by the probe tip lead to observable distortions in force maps, the extent of which increases with decreasing lateral stiffness. In

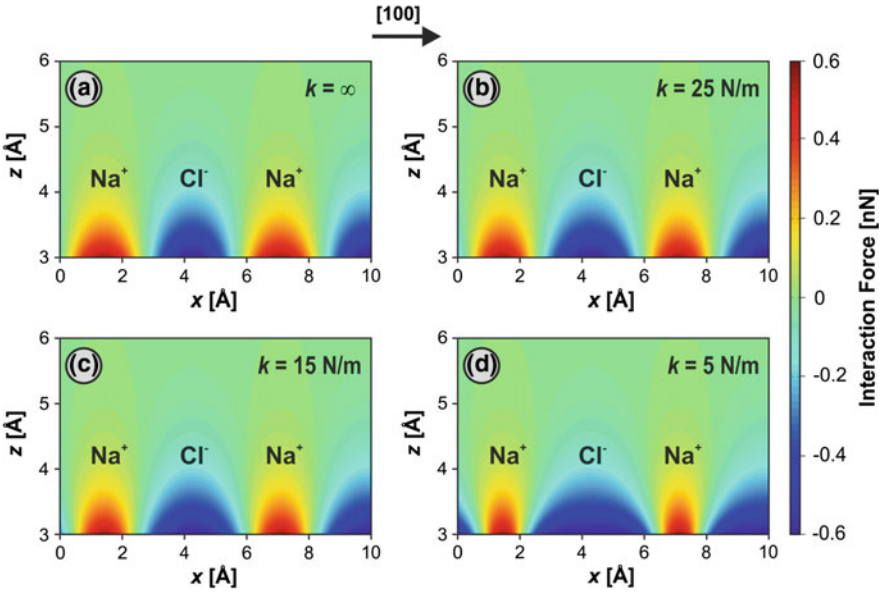

Fig. 2.5 2D maps of normal interaction forces on NaCl(001) calculated along the [100] direction for model Pt tip apices with lateral tip stiffness (k_{lateral}) values of ∞ (rigid tip), 25, 15, and 5 N/m. The distortions associated with the local force fields on Cl^- and Na^+ ions with decreasing tip stiffness can be clearly observed. Image reproduced from [42]

particular, repulsive force maxima situated on Na^+ ions become increasingly narrow with decreasing lateral stiffness and attractive force maxima on top of Cl^- ions become significantly wider. Taking into account that atomic-scale force spectroscopy and imaging experiments performed on ionic crystals often feature varying size and shape for the observed force maxima, the relevance of the results presented here in terms of the effect of tip elasticity on 3D force field spectroscopy becomes apparent.

2.4 Comparison of Data Acquisition and Processing Strategies for 3D Force Field Spectroscopy

Based on the information presented in this chapter so far, the various advantages and disadvantages of the methods established in the literature to perform 3D force field spectroscopy will be compared in this section. Towards this purpose, let us note that the main characteristics of the most commonly employed experimental methodologies for 3D force field spectroscopy can be summarized as:

- **Method A**: *Layer-by-layer* acquisition of data, post-data-acquisition drift correction, operation at low temperatures [26, 36]

- **Method B**: *Curve-by-curve* acquisition of data, atom-tracking/feedforward procedures, operation mostly at room temperature [30, 31, 33–35, 37]
- **Method C**: *Curve-by-curve* or *line-by-line* acquisition of data, use of a *reference image* for drift correction at fixed intervals during data acquisition, operation at low temperatures [27]

It should be noted though, that the three methods listed above represent a generalization at best and different combinations of approaches can be utilized in different experiments to address specific issues.

Using Table 2.1,

- All three methods satisfactorily address the effects of *thermal drift* and *piezo nonlinearities* on 3D force field spectroscopy.
- As *tip asymmetry* is an inherent issue associated with the probe tip itself, none of the presented methods are immune to its effects. Moreover, in the case of tip-sample interactions being predominantly short-range (see, e.g., the numerical simulation performed on Cu(001) and presented in Sect. 2.3.3), the post-data-acquisition correction of drift in the *layer-by-layer* approach becomes problematic as certain artifacts associated with tip asymmetry become indistinguishable from those related to thermal drift and elastic bending of the tip apex.

Table 2.1 Comparison of data acquisition and processing strategies for 3D force field spectroscopy

	Method A	Method B	Method C
Thermal drift	✓ Low thermal drift corrected post-acquisition	✓ Data acquisition has to be interrupted frequently to correct drift	✓ Data acquisition has to be interrupted to correct drift
Piezo nonlinearities	✓ Reduced piezo effects can be corrected post-acquisition	✓ Remaining piezo effects can be corrected post-acquisition	✓ Reduced piezo effects can be corrected post-acquisition
Tip elasticity	✓ Certain tip elasticity effects can be eliminated post-acquisition	×	×
Tip asymmetry	× May cause problems for post-acquisition drift correction on certain surfaces	×	×
Additional notes	Contrast distortions readily detectable during data acquisition	Irreversible tip changes much more likely at room temperature	–

- However, Method A holds a significant advantage over the other methods in case tip-sample interactions are predominantly long-range (as would be the case for most measurements performed on ionic crystals and metal oxides), since the post-data-acquisition correction procedures employed address both artifacts related to thermal drift as well as *elastic bending* of the tip apex towards a preferred direction due to normal forces (effect (a) discussed in Sect. 2.3.4, [43]).
- Another advantage of Method A over the other methods is the fact that irreversible changes in the tip apex are readily detectable during data acquisition in terms of changing image contrast whereas such observations cannot always be done in a straightforward fashion while data is collected *curve-by-curve*. Additionally, contrast changes with respect to changing tip-sample distance (such as those in [26, 32]) are directly observed during data acquisition, while such information only becomes observable after data processing in the case of *curve-by-curve* data acquisition.
- Despite the several advantages of Method A listed above when compared with the other data acquisition methods for 3D force field spectroscopy, it should be noted that the technique should not be employed when either (i) lateral drift between images is more than the lattice constant of the sample surface under investigation (unless a specific defect can be used as a *marker* of lateral position) and/or (ii) contrast patterns exhibit frequent changes with changing tip-sample distance such that alignment of features in subsequent images becomes problematic.

2.5 Combination of 3D Force Field Spectroscopy with Scanning Tunneling Microscopy: 3D-AFM/STM

A significant extension can be imparted on 3D force field spectroscopy via the recording of additional data channels such as energy dissipation and tunneling current during data acquisition [28]. While the recording of atomic-scale energy dissipation data during 3D force field spectroscopy has previously facilitated the identification of lattice sites on highly oriented pyrolytic graphite (HOPG) [26], the novel information that can be gathered regarding both the sample surface and the probe via the simultaneous recording of tunneling currents and interaction forces during 3D force field spectroscopy will be demonstrated in this section [36].

Simultaneous recording of interaction forces and tunneling currents is particularly interesting since information about atomic-scale reactivity of the surface and, at the same time, its electronic properties are collected to be contrasted and compared. Additionally, the data in the two channels can be utilized (i) to identify lattice sites on surfaces composed of multiple chemical species where symmetry arguments cannot be used in a straightforward fashion towards the same purpose and (ii) to uncover the structural and chemical characteristics of the probe tip apex, especially when the experimental data is interpreted in conjunction with ab initio simulations of interaction forces and tunneling currents.

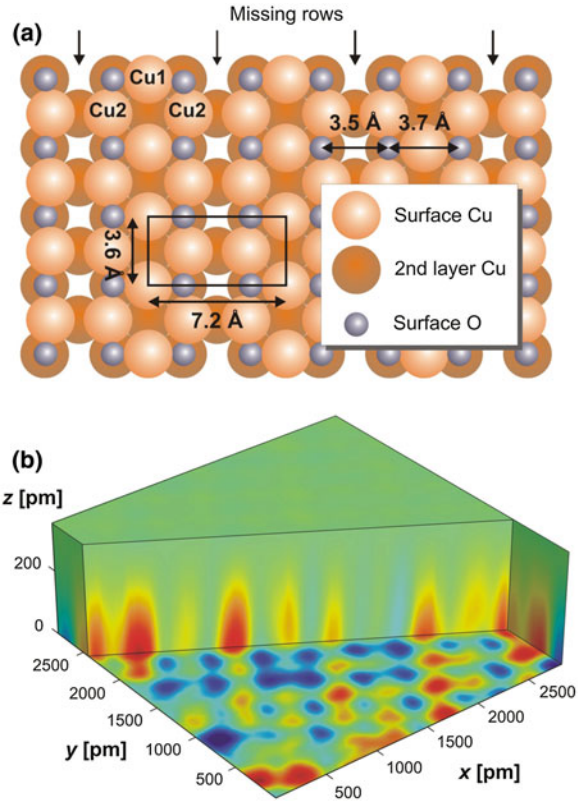

Fig. 2.6 **a** Reconstructed missing-row model of the surface oxide layer on Cu(100). Cu1 atoms are located at the centers of filled rows while Cu2 atoms are at the edges of troughs. **b** Three-dimensional representation of interaction forces measured on the sample surface using 3D force field spectroscopy. Atomic-scale features are clearly observed on the bottom plane. Image reproduced from [36]

To demonstrate the two points described above, a simultaneously recorded data set of interaction forces and tunneling currents on surface-oxidized Cu (100) is presented here [36]. The monolayer-thick surface oxide layer investigated in the experiments features a missing-row reconstruction where one in every four copper rows of the underlying substrate forms a trough, with filled rows between the troughs consisting of nearly co-planar Cu and O atoms in an alternating configuration (Fig. 2.6a). The combined 3D force field and tunneling current spectroscopy (3D-AFM/STM) experiments have been performed using a home-built, low temperature, ultrahigh vacuum instrument [23] equipped with a quartz tuning fork and an etched/field-ion beam treated Pt/Ir tip as the force sensor ($f_0 = 29{,}177\,\text{Hz}$, $A = 1.0\,\text{nm}$, $T = 5\,\text{K}$, bias voltage $U = -0.4\,\text{V}$, measurement time: 10 h). After drift correction performed according to *Method A* discussed in Sect. 2.4, the region of the surface over which the spectroscopy data is displayed comprises $2.89\,\text{nm} \times 2.89\,\text{nm}$.

The corresponding 3D force field spectroscopy data is displayed in Fig. 2.6b, where individual atomic-scale maxima can be observed in the bottom plane. Using the dense 3D information provided, the decay of interaction forces with increasing tip-sample distance as well as differences in interaction exhibited by different lattice

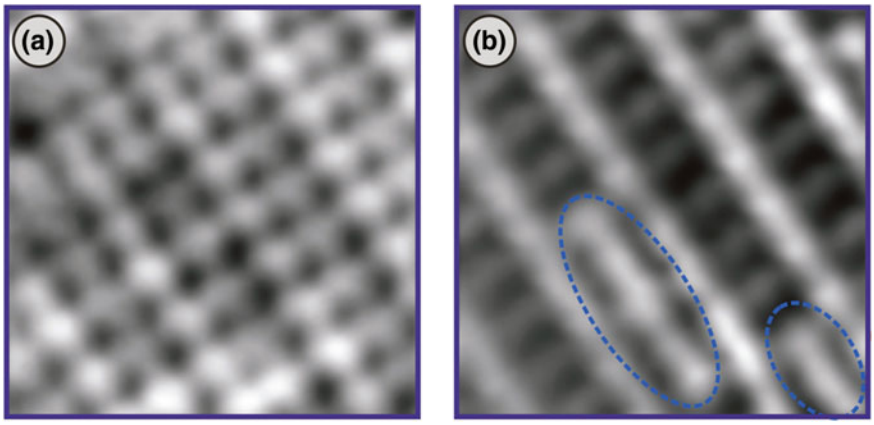

Fig. 2.7 **a** 2D map of interaction forces (2.89 nm × 2.89 nm) extracted from the 3D spectroscopy data in Fig. 2.6b at the bottom plane. Force maxima coincide with the O atoms on the surface. **b** 2D map of tunneling currents simultaneously acquired with interaction forces on the same plane. A *ladder-type* contrast is observed, coinciding with the copper atom arrangement on the surface. Surface defects in the form of partially filled troughs are highlighted. Image reproduced from [36]

sites can be studied with very high resolution. The magnitude of the maximum interaction force measured in the bottom plane is ∼1.34 nN whereas the contrast between atomically defined positions is ∼23 pN.

Employing a 2D map of interaction forces extracted from the 3D data set presented in Fig. 2.6b, force maxima can be unambiguously identified as the O atoms on the surface based on the symmetry of their arrangement (Fig. 2.7a). Surprisingly, the interaction force recorded for each O atom is different, with the values measured for different O atoms changing by as much as 40 % of the total force contrast on that plane. On the other hand, the map of tunneling currents simultaneously recorded at the same tip-sample separation features a very different, *ladder-like* symmetry, together with occasional linear defects imaged as partially *filled rows* on the troughs of the missing-row reconstruction (Fig. 2.7b).

To demonstrate the capability of identifying the structure and chemistry of the tip apex employed in the present 3D-AFM/STM experiment by a combination of experimental data with ab initio density functional theory simulations, force interactions of model tip apices involving Cu and O atoms with the sample surface as well as the associated tunneling currents are calculated. In the simulations, model tip apices consisting of Cu and O atoms are chosen due to the fact that tips have been treated by gentle crashes into the sample surface prior to data acquisition to improve imaging resolution in the experiments. A comparison of simulation results with experimental data then allows to determine that the tip apex used in the experiments is more than likely terminated by a Cu atom with an O atom adsorbed on the side (see inset in Fig. 2.8b), as this model apex successfully reproduces the experimentally obtained contrast in the tunneling current channel (where Cu1 atoms located at the centers of filled rows are imaged as bright protrusions and faint bridges of tunneling current are

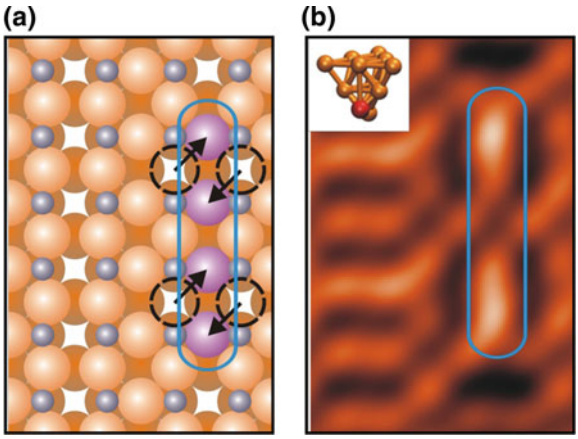

Fig. 2.8 **a** A surface defect model involving the displacement of two pairs of Cu2 atoms into the missing row. **b** The surface defect model presented in (**a**) is predicted to result in the observation of a linear defect in the tunneling current channel via ab initio simulations, in alignment with experimental data displayed in Fig. 2.7b. The *inset* in (**b**) represents the structural model of the tip apex used in the simulations. Image reproduced from [36]

formed by Cu2 atoms on both sides of the missing rows) and interacts most favorably with O atoms in the tip-sample distance regime of interest. *Simultaneous imaging of two different chemical species* via a combination of 3D force field spectroscopy and STM is demonstrated in this fashion.

Another aspect where the combined recording of interaction force and tunneling current data proves advantageous is the observation and identification of atomic-scale surface defects. In fact, the linear defect in the form of partially filled troughs observed in Fig. 2.7b would not have been detected if 3D force spectroscopy was being performed without simultaneous recording of the tunneling current channel, as the tip-sample interaction for the particular tip apex under consideration is dominated by O atoms. To identify the structural character of the defect under question, a number of defect models and the resulting simulations of tunneling current contrast were considered [36]. From the respective calculations, the atomic-scale origin of the linear defect observed in the current channel was established to involve the displacement of two pairs of Cu2 atoms into the missing rows (Fig. 2.8a). Based on this finding, it can be concluded that the variation of interaction force observed on each O atom is due to the variability in the chemical and electronic environment induced by the existence of surface defects, thereby providing direct, real-space evidence that surface defects affect chemical reactivity on the atomic scale [36].

As seen by the representative experiment discussed here, the combination of 3D force field spectroscopy with simultaneous recording of tunneling current (3D-AFM/STM) exhibits a tremendous potential for atomic-scale characterization of surfaces featuring multiple chemical species and even defects.

2.6 Conclusions and Outlook

The emerging method of 3D force field spectroscopy has been studied in this chapter, with particular attention paid to the different experimental methodologies proposed for data acquisition and processing. A discussion of common sources of artifacts in such measurements and the extent to which the proposed experimental methodologies address the related issues has been presented. The role that the probe itself plays on the acquired data, in terms of artifacts induced via asymmetry and elastic deformations has been investigated via numerical simulations involving basic pairwise potentials. Moreover, the combination of 3D force field spectroscopy with simultaneous recording of tunneling current has been demonstrated using experiments performed on surface-oxidized Cu(100). In particular, the advantages provided by such an approach in terms of the structural and chemical characterization of the tip apex, as well as the identification of individual lattice sites and even defects on the sample surface have been considered. Thereby, an interplay of experimental results and ab initio calculations proved crucial to achieve the indicated goals.

As the results presented in this chapter demonstrate, the data collected by 3D force field spectroscopy (and for that matter, any SPM technique) ultimately reflect a convolution of the physical properties of the surface with those of the probe tip. Since the aim of the 3D force field spectroscopy method is to uncover the atomic-scale properties of the surface itself, efforts towards standardization of probe tips are of utmost importance. While a significant amount of success has recently been achieved towards this goal via the deliberate functionalization of probe tips with molecules such as CO [27, 54], the next step in the development of the method towards increased functionality could involve functionalization of probe tips with molecules more relevant for practical processes such as catalysis and thin film growth. Despite the fact that such molecules are structurally more *complex* than CO and may, therefore potentially lead to certain other complications during experiments due to reduced structural rigidity, the results provided would open a new window to the world of chemical reactions on surfaces, as the actual force and energy landscapes that would be experienced by particular molecules relevant for practical processes can be visualized with unprecedented resolution via such an approach.

Acknowledgments The authors would like to thank Eric I. Altman, Omur E. Dagdeviren, Harry Mönig, Rubén Pérez, Lucia Rodrigo, Todd C. Schwendemann, Milica Todorović, Berkin Uluutku and Özhan Ünverdi for their invaluable contributions to the experimental and numerical studies presented in this chapter. Financial support from the National Science Foundation through the Yale Materials Research Science and Engineering Center (grant No. MRSEC DMR-1119826) and the Materials World Network program (grant No. MWN DMR-0806893) as well as the US Department of Energy (Basic Energy Sciences grant No. DE-FG02-06ER15834) are gratefully acknowledged. M.Z.B gratefully acknowledges support from the Turkish Academy of Sciences via the TÜBA-GEBİP program and the Marie Curie Actions of the European Commission's FP7 Program in the form of a Career Integration Grant (grant No. PCIG12-GA-2012-333843).

References

1. G. Binnig, H. Rohrer, Helvetica Physica Acta **55**, 726 (1982)
2. G. Binnig, C.F. Quate, C. Gerber, Phys. Rev. Lett. **56**, 930 (1986)
3. P.J. Eaton, P. West, *Atomic Force Microscopy* (Oxford University Press, Oxford, 2010)
4. F.J. Giessibl, Science **267**, 68 (1995)
5. Y. Sugawara, M. Ohta, H. Ueyama, S. Morita, Science **270**, 1646 (1995)
6. S. Morita, R. Wiesendanger, E. Meyer, *Noncontact Atomic Force Microscopy* (Springer, Berlin, 2002)
7. S. Morita, F.J. Giessibl, R. Wiesendanger, *Noncontact Atomic Force Microscopy* (Springer, Berlin, 2009)
8. T.R. Albrecht, P. Grutter, D. Horne, D. Rugar, J. Appl. Phys. **69**, 668 (1991)
9. M. Bammerlin, R. Luthi, E. Meyer, A. Baratoff, J. Lu, M. Guggisberg et al., Appl. Phys. A **66**, S293 (1998)
10. M. Reichling, C. Barth, Phys. Rev. Lett. **83**, 768 (1999)
11. R. Hoffmann, D. Weiner, A. Schirmeisen, A.S. Foster, Phys. Rev. B **80**, 115426 (2009)
12. C. Loppacher, M. Bammerlin, M. Guggisberg, S. Schar, R. Bennewitz, A. Baratoff et al., Phys. Rev. B **62**, 16944 (2000)
13. V. Caciuc, H. Hölscher, D. Weiner, H. Fuchs, A. Schirmeisen, Phys. Rev. B **77**, 045411 (2008)
14. T. Konig, G.H. Simon, H.P. Rust, M. Heyde, Appl. Phys. Lett. **95**, 083116 (2009)
15. J.V. Lauritsen, M. Reichling, J Phys.: Condens. Matter **22**, 263001 (2010)
16. M.P. Boneschanscher, J. van der Lit, Z.X. Sun, I. Swart, P. Liljeroth, D. Vanmaekelbergh, ACS Nano **6**, 10216 (2012)
17. Y. Dedkov, E. Voloshina, Phys. Chem. Chem. Phys. **16**, 3894 (2014)
18. Z. Majzik et al., J. Phys. Condens. Matter **25**, 225301 (2013)
19. H. Hölscher, A. Schwarz, W. Allers, U.D. Schwarz, R. Wiesendanger, Phys. Rev. B **61**, 12678 (2000)
20. M.A. Lantz, H.J. Hug, R. Hoffmann, P.J.A. van Schendel, P. Kappenberger, S. Martin et al., Science **291**, 2580 (2001)
21. Y. Sugimoto, P. Pou, M. Abe, P. Jelinek, R. Perez, S. Morita et al., Nature **446**, 64 (2007)
22. J.E. Sader, S.P. Jarvis, Appl. Phys. Lett. **84**, 1801 (2004)
23. B.J. Albers, M. Liebmann, T.C. Schwendemann, M.Z. Baykara, M. Heyde, M. Salmeron et al., Rev. Sci. Instrum. **79**, 033704 (2008)
24. M. Abe, Y. Sugimoto, O. Custance, S. Morita, Appl. Phys. Lett. **87**, 173503 (2005)
25. M. Abe, Y. Sugimoto, T. Namikawa, K. Morita, N. Oyabu, S. Morita, Appl. Phys. Lett. **90**, 203103 (2007)
26. B.J. Albers, T.C. Schwendemann, M.Z. Baykara, N. Pilet, M. Liebmann, E.I. Altman et al., Nat. Nanotechnol. **4**, 307 (2009)
27. L. Gross, F. Mohn, N. Moll, P. Liljeroth, G. Meyer, Science **325**, 1110 (2009)
28. M.Z. Baykara, T.C. Schwendemann, E.I. Altman, U.D. Schwarz, Adv. Mater. **22**, 2838 (2010)
29. B. Such, T. Glatzel, S. Kawai, S. Koch, E. Meyer, J. Vacuum Sci. Technol. B **28**, C4B1–C4B5 (2010)
30. S. Kawai, T. Glatzel, S. Koch, A. Baratoff, E. Meyer, Phys. Rev. B **83**, 035421 (2011)
31. S. Fremy, S. Kawai, R. Pawlak, T. Glatzel, A. Baratoff, E. Meyer, Nanotechnology **23**, 055401 (2012)
32. B. Such, T. Glatzel, S. Kawai, E. Meyer, R. Turansky, J. Brndiar et al., Nanotechnology **23**, 045705 (2012)
33. R. Pawlak, S. Kawai, S. Fremy, T. Glatzel, E. Meyer, ACS Nano **5**, 6349 (2011)
34. Y. Sugimoto, K. Ueda, M. Abe, S. Morita, J. Phys.: Condens. Matter **24**, 084008 (2012)
35. R. Pawlak, S. Kawai, S. Fremy, T. Glatzel, E. Meyer, J. Phys.: Condens. Matter **24**(8), 084005 (2012)
36. M.Z. Baykara, M. Todorovic, H. Monig, T.C. Schwendemann, O. Unverdi, L. Rodrigo et al., Phys. Rev. B **87**, 155414 (2013)

37. A.M. Sweetman et al., Nat. Commun. **5**, 7 (2014)
38. T. Fukuma, Y. Ueda, S. Yoshioka, H. Asakawa, Phys. Rev. Lett. **104**, 016101 (2010)
39. H. Asakawa, S. Yoshioka, K. Nishimura, T. Fukuma, ACS Nano **6**, 9013 (2012)
40. E.T. Herruzo, H. Asakawa, T. Fukuma, R. Garcia, Nanoscale **5**, 2678 (2013)
41. M.Z. Baykara, O.E. Dagdeviren, T.C. Schwendemann, H. Monig, E.I. Altman, U.D. Schwarz, Beilstein J. Nanotechnol. **3**, 637 (2012)
42. B. Uluutku, M.Z. Baykara, J. Vacuum Sci. Technol. B **31**, 041801 (2013)
43. B.J. Albers, T.C. Schwendemann, M.Z. Baykara, N. Pilet, M. Liebmann, E.I. Altman et al., Nanotechnology **20**, 264002 (2009)
44. S.O.R. Moheimani, Rev. Sci. Instrum. **79**, 071101 (2008)
45. H.J. Hug, B. Stiefel, P.J.A. van Schendel, A. Moser, S. Martin, H.J. Guntherodt, Rev. Sci. Instrum. **70**, 3625 (1999)
46. C.Z. Cai, X.Y. Chen, Q.Q. Shu, X.L. Zheng, Rev. Sci. Instrum. **63**, 5649 (1992)
47. W. Allers, A. Schwarz, U.D. Schwarz, R. Wiesendanger, Rev. Sci. Instrum. **69**, 221 (1998)
48. W.A. Hofer, A.S. Foster, A.L. Shluger, Rev. Mod. Phys. **75**, 1287 (2003)
49. N. Oyabu, P. Pou, Y. Sugimoto, P. Jelinek, M. Abe, S. Morita et al., Phys. Rev. Lett. **96**, 106101 (2006)
50. G.H. Enevoldsen, H.P. Pinto, A.S. Foster, M.C.R. Jensen, A. Kuhnle, M. Reichling et al., Phys. Rev. B **78**, 045416 (2008)
51. P. Pou, S.A. Ghasemi, P. Jelinek, T. Lenosky, S. Goedecker, R. Perez, Nanotechnology **20**, 264015 (2009)
52. H. Hölscher, W. Allers, U.D. Schwarz, A. Schwarz, R. Wiesendanger, Appl. Phys. A **72**, S35 (2001)
53. S. Kawai, T. Glatzel, S. Koch, B. Such, A. Baratoff, E. Meyer, Phys. Rev. B **81**, 085420 (2010)
54. J. Welker, A.J. Weymouth, F.J. Giessibl, ACS Nano **7**, 7377 (2013)